Applied Catalysis B: Environmental 338 (2023) 123028

Contents lists available at ScienceDirect

Applied Catalysis B: Environmental

journal homepage: www.elsevier.com/locate/apcatb

Conversion of polyethylene waste to short chain hydrocarbons under mild temperature and hydrogen pressure with metal-free and metal-loaded MFI zeolites

Jun Zhi Tan, Cole W. Hullfish, Yiteng Zheng, Bruce E. Koel, Michele L. Sarazen *

Department of Chemical and Biological Engineering, Princeton University, Princeton, NJ 08544, United States

ARTICLE INFO

Keywords:
Polyolefins
MFI
Bifunctional Catalysis
Hydrocracking

ABSTRACT

Catalytic hydrocracking on supported metal zeolites promisingly converts waste plastics into more valuable hydrocarbons. Although the presence of metal sites on solid acids is typically considered necessary for C-C bond cleavage of alkanes at modest temperatures, we show that polyethylene (PE) depolymerization on metal-free MFI zeolites proceeds at higher rates than analogous metal-loaded MFI zeolites (Pt, Ni) under mild reaction conditions. Higher rates on metal-free MFI are consistent with higher ratios of alkenes to alkanes, leading to subsequent alkene-mediated beta-scission events that form smaller molecules. Under varied reaction conditions (e.g., temperature, pressure, H_2 versus N_2), both metal-free and metal-loaded MFI catalysts demonstrate high selectivity to C_3-C_7 gaseous hydrocarbons, likely due to the 10-MR channel structure. Collectively, these findings demonstrate the importance of deconvoluting metal and acid sites contributions for PE hydrocracking, which has significant implications on rates and product selectivities of plastic upcycling reactions.

1. Introduction

In 2018, the majority of plastics that ended up as municipal solid waste in the U.S. were polyethylene (PE; 42%) and polypropylene (PP; 23%) [1], which are commonly utilized in single-use packaging. Mechanical recycling can recover some of the polyolefins produced, but these processes (e.g., extruding and grinding) typically degrade the mechanical properties of the original polymers, hindering their reusability for other applications [2,3]. In recent years, chemical upcycling, or advanced recycling, has emerged as a promising approach to recycle and reduce plastic waste [4–7]. Briefly, chemical upcycling utilizes thermochemical pathways to break down plastic waste into products of higher value (e.g., gasoline, diesel, and jet fuel) or into monomers for closed-carbon plastic production [8]. Some examples of common chemical upcycling strategies are thermal/catalytic pyrolysis, gasification, solvolysis, and hydroconversion (i.e., hydrocracking/hydrogenolysis) [4,5,9,10]. Among these techniques, pyrolysis has the highest technology readiness level [5], but produces a broad distribution of products (e.g., aromatics, cycloparaffins, olefins, and paraffins) and requires high energy costs due to high operating temperatures (>673 K) [11–17]. Due to these limitations, there is growing interest towards catalytic hydroconversion of plastic waste [18], which selectively forms linear and branched paraffins that require fewer subsequent processing units for fuel-based applications and can be performed under lower operating temperatures (≤573 K). This builds upon the rich history of hydrocracking, fluidized catalytic cracking, and hydrogenolysis of heavy oil components developed in the petroleum refining sector [19–22].

Solid acid catalysts such as crystalline zeolites [12,13,16,23], amorphous silica-aluminas [24–26], and (sulfated) metal oxides [27–29] in the absence of metals have been commonly utilized for catalytic valorization of polyolefins at high reaction temperatures (563–823 K), as their acid sites can protonate alkanes to form carbonium ions, which subsequently collapse to form carbenium ions that can be cleaved into smaller hydrocarbon fragments through beta-scission. Specifically, zeolites have been more extensively studied and utilized compared to other solid-acid catalysts due to their crystalline, microporous channels that provide size and shape selectivity for catalytic reactions and a tunable pore environment that can increase selectivity to desired products [30]. Although zeolites have been studied for decades in the context of alkane cracking, mechanistic insights related to accessibility of polymers into zeolite micropores remain unclear given the intrinsic, non-Newtonian nature of polymer melts and the high temperatures typically utilized for plastic pyrolysis. Since polyolefins

* Corresponding author.
E-mail address: msarazen@princeton.edu (M.L. Sarazen).

https://doi.org/10.1016/j.apcatb.2023.123028
Received 12 January 2023; Received in revised form 31 May 2023; Accepted 21 June 2023
Available online 23 June 2023

can thermally depolymerize into shorter-chain hydrocarbons under high temperatures (e.g., >673 K), this convolutes elucidation of whether the starting polymer melt can diffuse into zeolitic micropores.

Recent studies on polyolefin hydroconversion, which encompass both hydrogenolysis and hydrocracking, have demonstrated the prospect of utilizing monofunctional (only metal sites) and bifunctional (metal and acid sites) catalysts to cleave C-C bonds in waste plastics to yield liquid and gaseous hydrocarbons [31–46]. Typically, reaction temperatures for catalytic hydrocracking (<573 K) are lower than that for catalytic cracking, due to the presence of metal sites that can activate saturated alkanes. In general, Ru-based catalysts demonstrate superior performance over other metals (e.g., Pt, Ni, Pd) for C-C bond cleavage in terms of conversion rates, as demonstrated through hydrogenolysis studies done on commercial Ru/C, Pt/C, and Ni/C [31,45]. Unfortunately, the low regioselectivity for C-C bond cleavage of Ru-based monofunctional catalysts is detrimental to the value of the final products because of the large amount of methane (potent greenhouse gas) that is typically produced due to successive cleavage events (>80% selectivity). The pairing of Ru nanoparticles with solid acid catalysts (e.g., zeolites, oxides, and anion-modified zirconias) can slightly shift product distributions away from methane and produce heavier, branched liquid hydrocarbons [39,41,47], due to increased C-C bond cleavage through beta-scission in hydrocracking mechanisms. Notably, a physical mixture of FAU zeolite and Pt nanoparticles supported on tungstated zirconia shows much higher reactivity for PE conversion (6% solid residue) [40] than Pt/C (94% solid residue) [45] and produces a negligible amount of methane. The lower hydrogenolysis activity of Pt may render it more appropriate for polymer upcycling applications to mitigate production of methane [48]. Additionally, bifunctional Ni-based catalysts are also of interest, as Ni was previously shown to be moderately active for the hydrogenolysis and hydrodeoxygenation of biomass-derived compounds [49–52] and is significantly cheaper than noble metals that are frequently used in hydroconversion reactions.

Interestingly, metal-free zeolites were also shown to be active for catalytic cracking of PE under milder reaction conditions typically used for hydrocracking [38,53,54]. For instance, PE upcycling performed on mordenite framework inverted (MFI) zeolite nanosheets were shown to selectively produce C_1-C_7 light hydrocarbons (74.6% yield) in a flow reactor (553 K, 1 vol% H_2, 99 vol% N_2 and Ar) [53]. Metal-free MFI and Co-MFI catalysts were also shown to be active for conversion of PE to gaseous hydrocarbons (~84% C_3 on Co-MFI and H-MFI) under H_2 in a batch reactor setup (523 K, 40 bar H_2, 20 h), with slightly higher amount of unsaturated hydrocarbons observed on H-MFI than Co-MFI in the liquid phase [54]. In another study, conversion of n-hexadecane on metal-free MFI (13.7%) was shown to be higher than Co-MFI (1.9%) and Ni-MFI (2.2%) under batch conditions (548 K, 45 bar H_2, 2 h) [38]. Collectively, these findings challenge the notion that C-C chains along PE are first activated on the metal sites and diffuse to acid sites for C-C bond cleavage at lower temperatures (<573 K), as typically reported in a classical hydrocracking mechanism for gaseous and liquid alkanes (Scheme 1) [55]. Consequently, the initiation mechanism of PE on metal-free zeolites and the respective roles of metal and acid sites for polymer hydrocracking on metal-loaded zeolites remain elusive.

As described herein, we performed PE hydroconversion reactions (5–17 h) at mild temperatures (473–523 K) and pressures (10–30 bar initial H_2 or 10 bar initial N_2) on metal-free and metal-loaded MFI catalysts to elucidate the catalytic consequences of PE deconstruction on these catalysts. In this study, we define hydrocracking as reactions performed with bifunctional metal-loaded zeolites under a H_2 atmosphere and catalytic cracking as reactions performed with metal-free zeolites under either a H_2 or N_2 atmosphere. PE catalytic cracking reactions (473 K, 10 bar initial H_2, 5–17 h) were first performed on metal-free H-MFI zeolites with varying Si/Al ratios (40, 140, and ∞; where ∞ corresponds to Silicalite-1 (S-1)) to probe the reactivity of Brønsted acid sites for C-C bond cleavage. Next, PE hydrocracking reactions were performed on Pt and Ni independently deposited onto SiO_2 and MFI supports, respectively, under identical reaction conditions (473 K, 10 bar initial H_2, 12 h) to probe the reactivity of Pt- and Ni-loaded MFI for PE conversion. Systematic comparisons of solid conversions and product selectivities between metal-loaded MFI, metal-free MFI, and metal-only SiO_2 allow for decoupling of the respective contributions of metal and acid sites during PE hydrocracking reactions. The respective series of synthesized Pt and Ni catalysts has comparable metal nanoparticle size distributions across MFI and SiO_2 supports, which enables a more direct comparison of solid conversion due to smaller differences between type of exposed metal sites (e.g., terrace to edge ratio) and total exposed metal surface areas. Interestingly, the solid conversion (Eq. 1) of PE is higher on metal-free H-MFI-40 than on Pt/MFI-40 and Ni/MFI-40, which suggests mechanistic differences in C-C bond cleavage events on bifunctional metal-loaded catalysts compared to metal-free catalysts. Consequently, catalytic cracking reactions of PE on metal-free H-MFI-40 under different temperatures, pressures, and gas types (N_2 or H_2) were

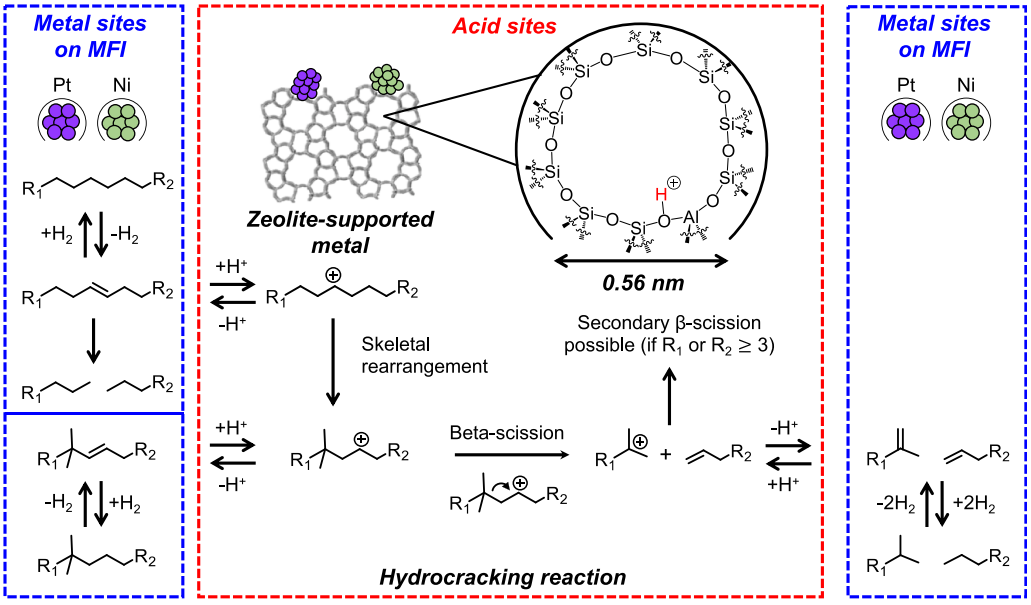

Scheme 1. Simplified schematic of hydrocracking over metal-loaded zeolites. R_1 and R_2 indicate additional carbon-carbon bonds.

performed to probe the mechanism of C-C bond cleavage. Thermogravimetric analysis (TGA) on a physical mixture of PE with 2,4,6-trimethylpyridine (TMP)-titrated parent H-MFI (external surface acid sites titrated) was also performed to elucidate the accessibility of PE into microporous voids of MFI. Collectively, results presented herein provide important insights into mechanistic differences between hydrocracking (on metal-loaded zeolites) and catalytic cracking (metal-free zeolites) of PE under H_2 environment, which have important implications for valorization of plastic waste.

2. Experimental methods

2.1. Preparation and synthesis of metal-free MFI zeolites

H-MFI-X, where X = nominal Si/Al ratio, and SiO_2 samples used in this study were either acquired from commercial sources or hydrothermally synthesized (Table 1). Commercial zeolites obtained in the NH_4^+-form were calcined for 8 h at 823 K (achieved by heating at 2 K min^{-1}) under dry air flow (Airgas, Ultra-zero grade; 150 cm^3 min^{-1}) to yield the protonated form. Silicalite-1 (S-1) was hydrothermally synthesized following procedures previously published (Section S1) [56].

2.2. Synthesis of supported metal catalysts

Pt and Ni metal nanoparticles (1 wt%) were independently deposited onto SiO_2 and H-MFI-40 supports via incipient wetness impregnation. For the synthesis of Pt-loaded SiO_2, the SiO_2 support (Sigma-Aldrich, Davisil Grade 646) was first treated for 5 h at 823 K (2 K min^{-1}) under flowing air (150 cm^3 min^{-1}). Briefly, for Pt/SiO_2, 0.027 g of $H_2PtCl_6{\cdot}(6\ H_2O)$ (Sigma-Aldrich, ≥37.5% Pt basis) was dissolved in 1.90 g of DI water and subsequently added dropwise to 1 g of SiO_2 under manual stirring with a plastic spatula. The metal-loaded SiO_2 was then heated to 393 K (1 K min^{-1}) and held for 8 h in a horizontal three-zone furnace under dry air (100 cm^3 min^{-1}) to remove excess water from the sample. After cooling to room temperature, the dried sample was heated in the same furnace to 673 K (2 K min^{-1}) under dry air (100 cm^3 min^{-1}) for 2 h and reduced at 673 K for 2 h under pure H_2 flow (Airgas, Ultra-high purity grade, 100 cm^3 min^{-1}). For Ni/SiO_2, the same procedure was followed except 0.050 g of $Ni(NO_3)_2{\cdot}(6\ H_2O)$ (Sigma-Aldrich, 99.999% trace metals basis) was used as the metal precursor.

Ni/SiO_2 was also synthesized via strong electrostatic adsorption (SEA) following a previously published procedure [57], as Ni/SiO_2 synthesized via incipient wetness impregnation has much larger particle sizes (7.7 ± 5.3 nm; data not included) than Ni/MFI-40 (2.6 ± 0.9 nm; Section 3.3), as determined by transmission electron microscopy (TEM). For SEA, Ni-containing solutions were prepared by dissolving 0.4954 g of $Ni(NO_3)_2{\cdot}(6\ H_2O)$ in a mixture of 200 mL 5 M NH_4OH and 300 mL DI water. Next, 250 mL of this solution was transferred to a 500 mL HDPE bottle and 1 g of fumed silica (Beantown Chemicals, 218810) was added to the solution. The solution was stirred at room temperature for 1 h, recovered via vacuum filtration, and air dried overnight. The dried Ni/SiO_2 was then heated to 393 K (1 K min^{-1}) and held for 4 h in a three-zone furnace under dry air flow (100 cm^3 min^{-1}), then ramped to 673 K (2 K min^{-1}) and held for 2 h under pure H_2 flow (100 cm^3 min^{-1}) to yield reduced Ni/SiO_2. Metal-loaded SiO_2 will be denoted as M/SiO_2 (where M = Pt or Ni).

Synthetic procedures of metal-loaded H-MFI-40 resembled that of Pt/SiO_2. Briefly, Pt and Ni metal nanoparticles were separately deposited onto H-MFI-40 by dissolving the respective metal precursors in volumes of DI water that corresponded to the pore volume of the zeolite support, followed by dropwise addition of this solution to the zeolite. The samples were dried at 353 K in an oven overnight, calcined at 673 K (2 K min^{-1}) for 2 h under air flow (100 cm^3 min^{-1}), and reduced at 673 K for 2 h under pure H_2 flow (100 cm^3 min^{-1}). Metal-loaded H-MFI-40 zeolites will be denoted as M/MFI-40 (where M = Pt or Ni), respectively.

Table 1
Source and Si/Al ratio of samples used in this study.

Catalyst	Source	Si/Al ratio
H-MFI-40	Zeolyst (CBV 8014)	40[a]
H-MFI-140	Zeolyst (CBV 28014)	140[a]
S-1	Hydrothermal synthesis [56]	∞
SiO_2	Sigma-Aldrich (Davisil Grade 646)	∞
SiO_2	Beantown Chemical (218810)	∞

[a] Specified by vendor

2.3. Characterization of materials

Material and active site characterizations were performed on procured and synthesized catalysts. X-ray diffractograms (XRD) on MFI catalysts were collected with a diffractometer (Bruker, D8 Discover) under Cu Kα radiation (0.15418 nm) at a scan rate of 5° min^{-1} under ambient conditions. The resemblance between diffractograms of metal-free MFI zeolites (H-MFI-40 and S-1) with those of metal-loaded MFI zeolites (Pt/MFI-40 and Ni/MFI-40, Fig. S1) indicate that metal incorporation and subsequent calcination and reduction treatment do not affect crystallinity of the MFI zeolite and that S-1 possessing MFI framework was successfully synthesized.

NH_3-temperature programmed desorption (TPD) was carried out with a chemisorption analyzer (Micromeritics, AutoChem II) to determine the density of weak and strong acid sites of the zeolites. The samples were first pretreated in situ under He flow (Airgas, Ultrahigh purity grade, 30 cm^3 min^{-1}) at 673 K (10 K min^{-1}) for 1 h, then cooled to 373 K. At 373 K, the gas flow was switched to 10% NH_3 (balance He; Airgas, 30 cm^3 min^{-1}) to allow for adsorption of NH_3 for 2 h. Subsequently, the gas flow was switched back to He to desorb weakly adsorbed NH_3 for 1 h. Lastly, the sample was ramped from 373 K to 973 K (10 K min^{-1}) under He flow, and the amount of adsorbed NH_3 was determined with a thermal conductivity detector (TCD). The NH_3-TPD curves of MFI samples show two desorption features (Fig. S2), where the desorption feature at lower temperature and higher temperature is typically associated with weak and strong acid sites, respectively. Although NH_3-TPD cannot fully distinguish Lewis and Brønsted acid sites, the density of strong acid sites determined from NH_3-TPD on H-MFI-40 materials (density of strong acid sites = 0.35 mmol g^{-1}) is consistent with our TPD results on NH_4^+-exchanged metal-free MFI-40 (density of BAS = 0.32 mmol g^{-1}) using procedures previously described [58] and with those published in literature (utilizing isopropylamine titration or pyridine-FTIR) on commercial H-MFI-40 (density of BAS = 0.33–0.34 mmol g^{-1}) [59,60]. Consequently, NH_3-TPD is utilized here to provide semi-quantitative assessment of the density of BAS on the MFI samples.

N_2 physisorption isotherms at 77 K were obtained on an adsorption analyzer (Micromeritics, 3Flex) to determine the pore volumes of the metal-free and metal-loaded MFI samples (Fig. S3). The samples were degassed at 393 K under vacuum (125 Torr) overnight with a Schlenk line prior to N_2 physisorption experiments. Micropore volume (V_{micro}) and surface area (S_{micro}) of the samples were determined from the t-plot method (Table 2 and S1; Harkins-Jura model; t = 3.5–5 Å; P/P_0 = 0.06–0.3) [61], while mesopore volume (V_{meso}) and surface area (S_{meso}) were determined from the BJH adsorption curve (Table S1; Harkins-Jura model, Faas correction, 2–50 nm).

CO-pulse chemisorption and TEM were used to determine the metal particle size distribution of metal-loaded samples. For CO-pulse chemisorption, the samples were pretreated in situ under 10% H_2 (balance Ar; Airgas, 50 cm^3 min^{-1}) at 673 K (10 K min^{-1}) for 0.5 h. The gas flow was then switched to He and the samples were held at 673 K for another 0.5 h to desorb adsorbed H_2. After 0.5 h, the sample was cooled to 323 K and held at this temperature for 10 min. Once the baseline of the TCD detector was stabilized, 10% CO (balance He; Airgas) was injected from

Table 2
Micropore volumes and density of acid sites of metal-free and metal-loaded MFI catalysts.

Catalyst	Micropore volume[a] ($cm^3\ g^{-1}$)	Density of weak acid sites[b] ($mmol\ g^{-1}$)	Density of Brønsted acid sites[c] ($mmol\ g^{-1}$)
H-MFI-40	0.13	0.29	0.35
H-MFI-140	-	0.05	0.08
Pt/MFI-40	0.12	0.37	0.45
Ni/MFI-40	0.12	0.28	0.33

[a]Determined from t-plot analysis.
Determined from [b]low-temperature and [c]high-temperature feature on NH_3-TPD curve.

the sampling loop (0.51 cm^3) every 6 min until the peaks were equal or after 10 injections were done. TEM images were obtained with a TEM (Talos, F200X) at 200 keV acceleration voltage. Briefly, catalyst samples (1 mg) were dissolved in 5 mL of ethanol solution (Sigma-Aldrich, 200 proof, ≥99.5%) and sonicated for 0.5 h before deposition onto a TEM copper mesh grid (Sigma-Aldrich, FCF400). The copper mesh grid was then mounted onto a single-tilt TEM holder and loaded into the electron microscope for analysis.

2.4. Batch hydrogenolysis and hydrocracking experiments on PE

Solvent-free catalytic hydrocracking and cracking reactions of commercial polyethylene (Sigma-Aldrich, 4000 Da) were carried out in a batch stainless steel reactor (Parr Instrument, 450 mL, Series 4567) without stirring. Fig. S4 shows a schematic of the reactor configuration. First, desired ratios of catalyst and commercial PE (typically 1:5 catalyst to PE ratio) were ground together with a mortar and pestle and loaded into the reactor. The reactor was purged with continuous N_2 gas flow (Airgas, Ultrahigh purity grade) for 5 min after loading the solid mixtures, then cyclically purged and charged five times with H_2 (Airgas, Ultrahigh purity grade) gas at the desired reaction pressure before starting the experiment. The reactor pressure was measured with a pressure transducer (Dwyer, Series 626). The reactor was then heated to the desired temperature with a cylindrical heater (Parr Instrument, A2230HC2EB). The temperature of the reactor was controlled with a heat controller (Omega, CND3) connected to an internal thermocouple (Parr Instrument, type K) positioned slightly above the solids (~1–2 cm). After reaction, the reactor vessel was immediately cooled to a temperature below 283 K in an ice bath before gases in the headspace were collected in a gas bag through a bleed valve connected to the reactor. Gaseous products were characterized via direct injection with a gas-tight syringe (Hamilton, 81320) into a custom-designed direct injection port (Fig. S5), which is connected to a gas sampling valve (250 μL) on a gas chromatograph (Thermo Scientific, Trace 1300) equipped with a Rt-Q-BOND column (Restek, 30 m × 0.32 mm × 10 μm) and flame ionization detector (FID). Response factors for gaseous products were obtained by both direct flow of pure alkane gases (C_1-C_3) and direct injection of a C_1-C_6 standard gas mixture (balance H_2; Airgas; 83.2 mol% H_2, 5.004 mol% CH_4, 5.020 mol% C_2H_6, 5.017 mol% C_3H_8, 1.002 mol% C_4H_{10}, 0.5026 mol% C_5H_{12}, 0.2520% C_6H_{14}) to the FID. The response factors obtained from both methods were similar. Liquid products were recovered from the reactor with 20 mL of dichloromethane (DCM) and characterized with GC-FID and ^1H NMR. For ^1H NMR, 45 μL of the recovered solution was diluted with 555 μL $CDCl_3$ (Sigma-Aldrich, 99.8% atom D) and analyzed (Bruker, 500 MHz) to detect the presence of aromatics. For GC-FID characterization, 5 μL of mesitylene was added to the recovered liquid solution and injected (1 μL) into a split/splitless inlet on a gas chromatograph (Agilent, 7890 A) equipped with a HP-5 column (Agilent, 30 m × 0.32 mm × 0.25 μm) and FID. Response factors for liquid products (C_8-C_{40}) were obtained by utilizing standard solutions of C_8-C_{20} (Sigma-Aldrich, 04070) and C_{21}-C_{40} (Sigma-Aldrich, 04071) alkanes and confirmed with C_8 (Sigma-Aldrich, 74821), C_{10} (Fisher Scientific, O2128), and C_{16} (Sigma-Aldrich, H6703) pure alkanes. Solid residues in the Parr reactor were recovered with ~40–50 mL of acetone and poured into a pre-weighed beaker to maximize recovery of solid residues and obtain more accurate weight measurements. The suspension of acetone and solid residues was completely dried on a heated stir plate at 323 K for > 4 h and massed. The mass of the solid residue was used to determine the solid conversion, which is defined as:

$$\text{Solid conversion}(\%) = \frac{m_{PE} - (m_{\text{solid residue}} - m_{\text{catalyst}})}{m_{PE}} \times 100\% \quad (1)$$

where m_{PE}, $m_{\text{solid residue}}$, and m_{catalyst} is the initial mass of PE, mass of solid residue after reaction, and initial mass of catalyst, respectively. Figs. S6-S8 show and discuss mass balances for all reactions in this study.

2.5. Thermogravimetric analysis on PE + parent/titrated MFI zeolites

Thermogravimetric analysis (TGA) was performed (PerkinElmer, TGA 8000) to study catalytic cracking of PE under an inert environment with fresh and 2,4,6-TMP titrated MFI zeolites. Metal-free MFI zeolite (50 mg) was titrated with 2,4,6-TMP (100 mg) in a scintillation vial and dried under ambient conditions overnight. For catalytic cracking experiments, 8–15 mg of physically mixed PE and MFI zeolites (5:1 PE to catalyst ratio) was loaded onto a ceramic pan. The experiments were performed under Ar flow (Airgas, Ultrahigh purity grade, 30 $cm^3\ min^{-1}$) and ramped from 303 K to 423 K (10 K min^{-1}; held for 2 h) to remove moisture (or physisorbed TMP) from the catalysts. After 2 h, the temperature was ramped to the desired reaction temperature (i.e., 523 K) and held for 5 h to mimic catalytic cracking in batch reactions (Section 2.4).

3. Results and discussion

3.1. Activation of PE with metal-free H-MFI under mild reaction conditions

Catalytic cracking reactions of PE under H_2 were performed on metal-free H-MFI zeolites of different Si/Al ratios to probe the

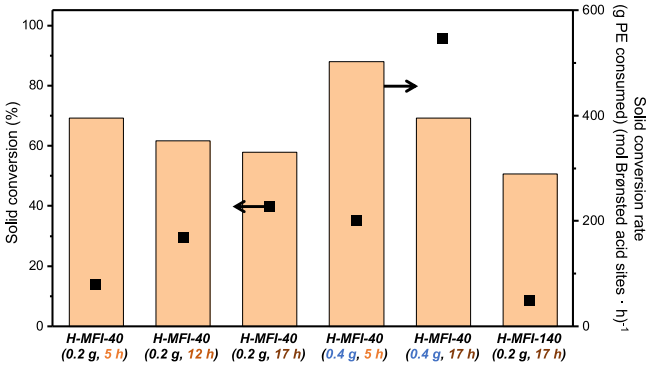

Fig. 1. Solid conversion (■) and solid conversion rate (bar) of PE catalytic cracking on metal-free MFI zeolites under varying reaction time, catalyst loading, and Si/Al ratio. Reaction time and mass of catalyst added are shown in bar label. Reaction condition: 473 K, 10 bar initial H_2 pressure, and 1 g PE.

independent role of Brønsted acid site density. Fig. 1 shows the solid conversion and solid conversion rate of PE hydrocracking on metal-free MFI samples. Here, we utilize solid conversion (Eq. 1) and solid conversion rate as a source of comparison across different experiments, where solid conversion indicates the amount of solid PE that is converted into gaseous or liquid products while solid conversion rate is the mass of PE consumed normalized by the moles of Brønsted acid sites and unit time. We note that these metrics, however, do not account for transformation of PE into lower molecular weight or branched solid PE. Of the MFI catalysts analyzed in this section, generally small amount of liquid products (<30 mg) was produced for reactions with solid conversions in the lower range (<40%) (Fig. S6a), and the liquid products consisted of mainly C_7-C_{10} hydrocarbons with trace amount of C_{11}-C_{15} hydrocarbons (Fig. S9). Even at higher solid conversion (96%), only 80 mg of liquid product was obtained (Figs. S6a and S8d), and the liquid product distribution remains similar to those obtained at lower solid conversions (<40%; Fig. S9). Since the majority of products produced were gaseous hydrocarbons in the C_3-C_7 range (~5x more gaseous products by mass) despite underestimation of total gaseous products mass (Section S3 and Fig. S10), gaseous yields are used to analyze product selectivities on this suite of catalysts.

Unexpectedly, even under mild temperature and H_2 pressure (473 K, 10 bar initial H_2 pressure), non-negligible solid conversion (14%) was observed on H-MFI-40 after 5 h (Fig. 1). Appropriate control reactions were completed to verify that the PE degradation is due to the presence of H-MFI-40, including a blank reaction with 1 g PE that gave about 5% solid conversion (Fig. S11), which can be accounted for by the minor loss of solid products (50 mg) during the recovery process. Nonetheless, the solid conversion observed on H-MFI-40 is significantly greater than that of pure PE without any catalyst, consistent with the involvement of acid sites in cracking. Additionally, a n-hexane blank experiment performed (473 K, 10 bar initial H_2, 20 h) in the absence of any catalysts within the Parr reactor yielded only n-hexane (without any alkenes), which indicates an insignificant presence of metal contaminants in the reactor that could convert alkanes to alkenes (Fig. S12). Although protolytic cracking of alkanes on monofunctional acidic zeolites has been reported in prior studies [62–66], these examples were run at much higher temperatures (>673 K) than that used in this study (473 K). Since intrinsic cracking reactivities of n-alkanes typically increase with carbon number and branching due to higher equilibrium adsorption constants and higher reactivity of tertiary C-H bonds [65,67,68], respectively, it is possible that the long carbon chain and branching points in PE lower the reaction temperature needed for alkane activation on the MFI zeolites. Catalytic cracking reaction of larger molecular weight PE (M_w ~ 76 kDa based on ref [39,42], Sigma-Aldrich, 428043) with H-MFI-40 under H_2 environment was also performed and yielded 17% solid conversion after 17 h, indicating that this is not sample dependent (Fig. S13). The lower solid conversion of 76 kDa PE compared to 4 kDa PE is likely due to higher melting point (389 K for 76 kDa PE and 369 K for 4 kDa PE) of the 76 kDa PE, which would likely reduce the diffusivity of the polymer wax. Even without these differences, more C-C bond scission events are needed to convert solid 76 kDa PE to shorter-chain hydrocarbons (liquid or gaseous) than 4 kDa PE, which would manifest as lower solid conversion at the same clock time, since scission events that produce shorter chain solid products are not accounted for when using solid conversion as a metric for comparison.

On H-MFI-140, solid conversion of 4 kDa PE is lower than on parent H-MFI-40 by 31% due to the lower Brønsted acid site density (Fig. 1). Reactions of PE + SiO_2 and PE + S-1 were also carried out to determine the solid conversion and product yield on the inert SiO_2 support and the MFI framework without Brønsted acid sites. For these reactions, solid conversions were around 5% with only trace amounts of gaseous products formed (Fig. S11), similar to result from the blank PE reaction. The similarity in solid conversion observed on PE + S-1 with those of the blank PE (without catalyst) and PE + SiO_2 indicate that confinement effects alone are not strong enough to cleave C-C bonds in the PE chain, and thus the high solid conversion observed on metal-free H-MFI-40 is mainly due to the presence of Brønsted acid sites.

Catalytic cracking reactions performed on metal-free H-MFI-40 (1:5 catalyst to PE ratio) at varying reaction times (5–17 h) show that solid conversion gradually increases from 14% to 40% with increasing reaction time (Fig. 1). Solid conversion rates are within similar ranges for the different reaction times probed at 1:5 catalyst to PE ratio (<1.2 times difference). Doubling the H-MFI-40 catalyst to PE ratio (from 1:5–2:5) increases solid conversion by 21% and 56% at 5 h and 17 h (Fig. 1), respectively, while solid conversion rates remain in a similar range (<1.3 times difference) at different reaction times. The slight decrease in solid conversion rates with increasing reaction time could be due to decreasing reactant concentration and slight deactivation (e.g., pore blockage), while the slightly higher solid conversion rates obtained when the catalyst to PE ratio is doubled may be associated with more (surface) acid sites that can facilitate C-C bond cleavage of long chain PE into a pool of shorter-chain hydrocarbons at higher rates. On H-MFI-140, the solid conversion rate (290 $\frac{g\ PE\ consumed}{mol\ Brønsted\ acid\ sites \bullet h}$) was also similar to that on H-MFI-40 (330 $\frac{g\ PE\ consumed}{mol\ Brønsted\ acid\ sites \bullet h}$). Taken together, utilization of solid conversion rates to compare between varying ratios of H-MFI-40 to PE, differing Si/Al ratios of H-MFI, and increasing reaction time, indicate that the differences in solid conversion observed in Fig. 1 mainly originate from differences in Brønsted acid site density.

Fig. 2 shows that the mole percent of C_1-C_7 gaseous products from PE + H-MFI-40 under different reaction times and different catalyst to PE ratios (i.e., 1:5 and 2:5) do not vary significantly (1.3–1.7 mol% C_1-C_2, 21–25 mol% C_3, 74–77 mol% C_4-C_7). This indicates that gaseous product selectivities do not vary significantly with solid conversion (14–96%) under the reaction conditions tested. Interestingly, alkene products were also observed, albeit at lower amount compared to alkanes (e.g., measured alkane/alkene mole ratios for C_3 and linear C_4 are 26:1 and 11:1, respectively). On H-MFI-140, the gaseous product selectivities (1.7 mol% C_1-C_2, 26 mol% C_3, 73 mol% C_4-C_7) are similar to that of H-MFI-40 (1.3 mol% C_1-C_2, 22 mol% C_3, 77 mol% C_4-C_7) at t = 17 h, but the linear to iso ratios of H-MFI-140 are slightly higher than that of H-MFI-40 (e.g., mole ratio of n-butane to isobutane is 3.0:1 and 1.8:1 on H-MFI-140 and H-MFI-40, respectively). The difference in linear to iso ratio could be due to higher density of Brønsted acid sites within H-MFI-40 compared to H-MFI-140 that increases intracrystalline residence time of alkenes (and thus isomerization rates) [69], as was shown by the higher rate constants for n-heptane isomerization in bifunctional Pt/SiO_2 + MFI zeolites in a previous study [70]. In terms of liquid products, although the recovered solution remains clear (i.e., no polycyclic aromatics) for H-MFI-40 at 1:5 catalyst to PE ratio from 5 to 17 h (Fig. S14), small amount (<4.4 mg) of aromatics (i.e., benzene) was observed in the recovered liquid solution by ^{1}H NMR analysis (Fig. S15 and Table S2). For 2:5 catalyst to PE ratio (5 and 17 h), the amount of aromatics produced is in similar ranges (Fig. S16 and Table S3), but the recovered solution is slightly yellowish likely due to presence of polycyclic aromatics (e.g., pyrene) that could produce a yellowish color at trace concentrations (Fig. S17). Taken together, results from ^{1}H NMR show that small amount of aromatics were formed within the liquid solution at mild reaction temperatures (473 K), and that higher catalyst loading and increasing reaction time produce more aromatics and more substituted aromatic rings, respectively.

Low selectivity of C_1-C_2 products (1.3–1.7 mol%) for experiments performed on H-MFI-40 (Fig. 2) suggests that the catalytic cracking of PE on MFI zeolite proceeds primarily through bimolecular cracking or beta-scission pathways as opposed to monomolecular cracking, based on beta-scission mechanisms during alkene oligomerization that do not form C_1-C_2 products [58]. If monomolecular cracking was the dominant pathway, more C_1-C_2 products would likely be observed, according to an earlier study on n-hexane cracking with H-MFI at 10 kPa n-hexane partial pressure and 723 K [71]. However, without a dehydrogenation component (e.g., metal sites), it is not immediately clear how C-C bonds

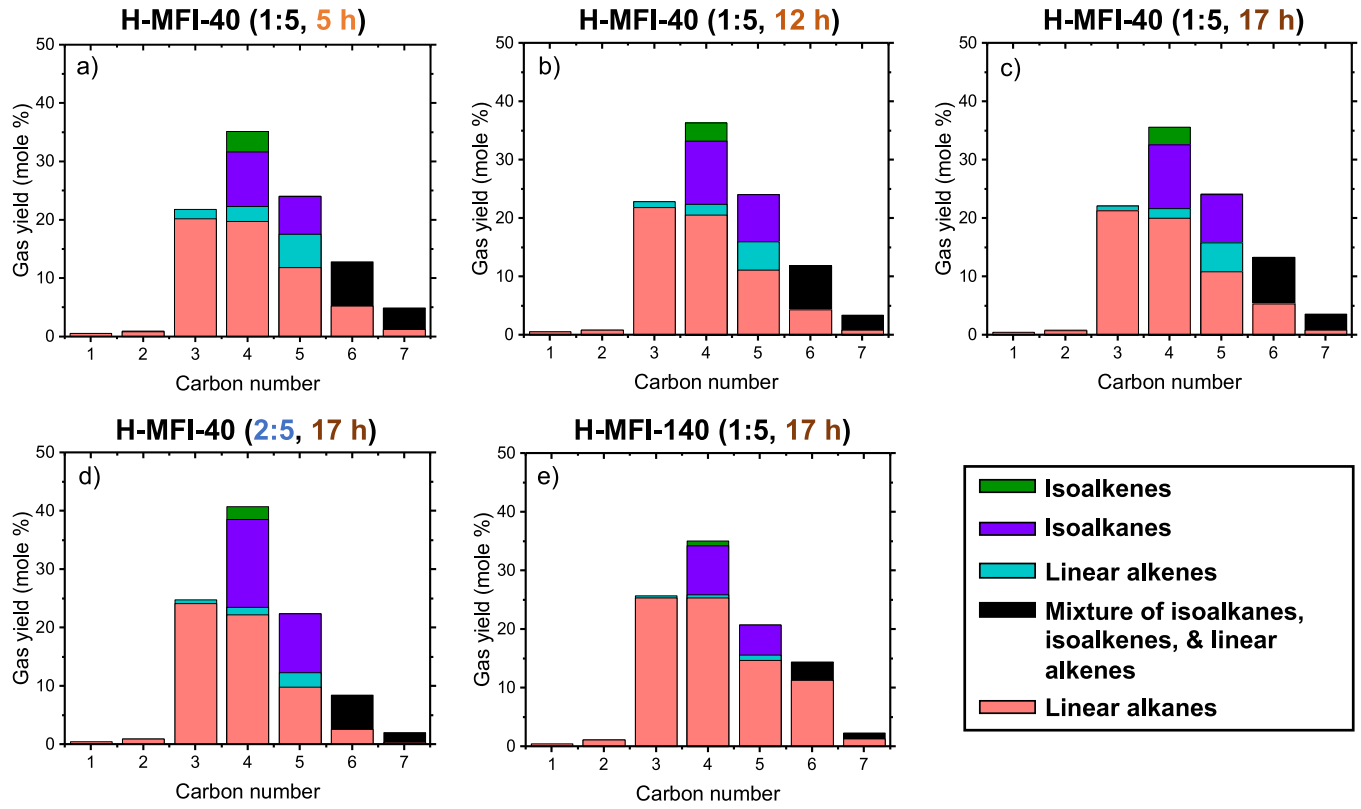

Fig. 2. Gaseous product yield (as mole percent) of (a) H-MFI-40 (1:5 catalyst to PE ratio; 5 h), (b) H-MFI-40 (1:5 catalyst to PE ratio; 12 h), (c) H-MFI-40 (1:5 catalyst to PE ratio; 17 h), (d) H-MFI-40 (2:5 catalyst to PE ratio; 17 h), and (e) H-MFI-140 (1:5 catalyst to PE ratio; 17 h). Reaction condition: 473 K, 10 bar initial H_2 pressure, and 1 g PE. Pink, blue, purple, and green bars indicate linear alkanes, linear alkenes, isoalkanes, and isoalkenes, respectively. Black bars indicate a mixture of isoalkanes, isoalkenes, and linear alkenes for C_6-C_7 with overlapping GC peaks.

in PE can be activated to alkenes to this extent at these temperatures. We can propose two possible mechanisms for the initiation steps. First, alkane segments along the PE chain can be activated to a certain extent at mild temperatures (following a monomolecular cracking mechanism), producing C_1-C_2 hydrocarbons and carbenium ions that can undergo subsequent beta-scission. Second, if weak links (e.g., branching points, alkene, carbonyl) are present across the commercial PE chain, the activation barriers for formation of carbenium ions from these weak links after protonation are much lower than from linear alkanes, which allows for subsequent beta-scission into shorter hydrocarbon fragments (Scheme 1). We note that these proposed initiation mechanisms are not necessarily mutually exclusive and will be further probed in the next section.

3.2. *Elucidation of reaction mechanism for PE catalytic cracking on metal-free H-MFI-40*

Catalytic cracking reactions of PE were performed at different reaction temperatures, pressures, and gaseous environment (H_2 or N_2) on metal-free H-MFI-40 to elucidate the potential mechanisms of C-C bond cleavage on metal-free zeolites and identify optimum reaction conditions. As the temperature increases from 473 K to 523 K at 5 h reaction

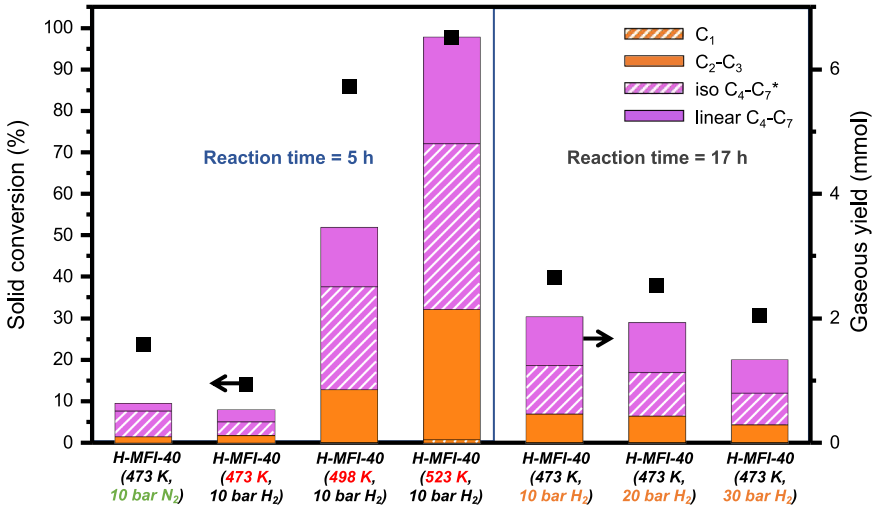

Fig. 3. Solid conversion (■) and gaseous product yield (in mmol; bars) of PE catalytic cracking on metal-free H-MFI-40 under varying reaction temperatures, pressures, and gas compositions (shown in bar labels; 1 g PE and 0.2 g catalyst). Blue background (left) indicates that the reaction was performed for 5 h while grey background (right) indicates that the reaction was performed for 17 h. Orange and purple solid bars indicate C_2-C_3 and C_4-C_7 linear alkanes, respectively, while orange and purple striped bars indicate C_1 and C_4-C_7 isoalkanes, respectively. The asterisk next to the iso C_4-C_7 label indicates that C_4-C_7 alkenes are also present and included under this value.

time under H_2 environment (10 bar initial H_2), solid conversion on H-MFI-40 increases by 84% (Fig. 3) and the gaseous product distribution gradually shifts from C_4-C_7 to lighter C_3 hydrocarbons (22 mol% C_3 at 473 K to 35 mol% C_3 at 523 K; Figs. S18 and S19). This shift is due to an increase in temperature instead of solid conversion, as gaseous product selectivity remains similar on H-MFI-40 across different solid conversion ranges at 473 K (14–96%; Fig. 2). Specifically, the moles of C_1 and C_2 hydrocarbons produced on H-MFI-40 at 523 K is 9x and 19x greater than at 473 K, respectively (Fig. S20). The larger amount of C_1-C_2 hydrocarbons produced with increasing temperature suggests that protolytic cracking is likely one of the pathways responsible for C-C bond cleavage on PE, since beta-scission alone cannot produce gaseous hydrocarbons that are shorter than C_3, due to the required formation of unstable primary carbenium ions. However, as gaseous product distributions across the range of temperatures tested (473–523 K) are still mainly C_3-C_7 hydrocarbons (from beta-scission), protolytic cracking is unlikely to be the dominant pathway for the majority of the C-C bond cleavage events. In terms of liquid products, the mass obtained increased from 5 mg to 173 mg when temperature increases from 473 K to 523 K (Fig. S21), but the liquid product selectivities remain similar with those observed in Section 3.1 (i.e., mainly C_7-C_{10} hydrocarbons with smaller amount of C_{11}-C_{15} hydrocarbons). The color of the recovered liquid solution also turns light yellow with increasing temperature (Fig. S22), indicating an increase in the amount of aromatics (e.g., alkylaromatics or polyaromatics) formed, consistent with results from ^{1}H NMR analysis (Fig. S23 and Table S4). This indicates that for plastic upcycling reactions on metal-free MFI, higher reaction temperatures will lead to increased selectivity to aromatic compounds, which agrees with results observed from catalytic conversion of gaseous hydrocarbons [72–74].

Solid conversion on H-MFI-40 is 10% lower at 30 bar initial H_2 pressure than that at 10 bar (Fig. 3), while the gaseous product selectivity remains similar across the pressure range (Figs. 3 and S19). As the initial H_2 pressure increases from 10 to 30 bar, the mole ratios of alkane to alkene increased (specifically, propane to propene, butane to butene, and isobutane to isobutene, increased from 35:1–91:1, 12:1–34:1, and 4:1–13:1, respectively). This suggests that higher pressure of H_2 hydrogenates the alkene pool to a larger extent, which consequently leads to lower solid conversion as beta-scission active alkenes are scavenged. Catalytic hydrogenation of alkenes to alkanes under a H_2 environment has been shown in an earlier study with propene on metal-free MFI zeolite at 743 K (SiAl = 16.5), where the reaction was proposed to proceed via the microscopic reverse of monomolecular alkane dehydrogenation pathways through carbonium-ion like transition states [75]. Additionally, protolytic propene hydrogenation rates were shown to increase concomitantly with H_2 pressure [75], consistent with our results presented herein. Consequently, these results suggest that the metal-free zeolite plays a role in facilitating hydrogenation even in the absence of metal sites.

Catalytic cracking on H-MFI-40 were performed under varying gas compositions (10 bar H_2 or 10 bar N_2) but identical reaction conditions (473 K and 5 h; Fig. 3) to further elucidate the impact of alkenes under the reaction conditions used in this study. The solid conversion on H-MFI-40 increases by 10% under 10 bar N_2 compared to H_2, which is consistent with higher amounts of beta-scission-active alkenes in the pool of hydrocarbons during catalytic cracking (Figs. 4 and S24). Indeed, the measured alkane to alkene mole ratios are lower in a N_2 environment than in a H_2 environment (specially, propane to propene, butane to butene, isobutane to isobutene, decreased from 12:1–1:1, 2.6:1–0.5:1, and 7.7:1–0.7:1). Interestingly, catalytic cracking of PE at mild temperatures under a N_2 environment only produce small amount of aromatics at 5 h reaction time (Figs. S25 and S26), similar to that observed under H_2 environment (Table S5). This is in contrast with pyrolysis studies of PE under N_2 at elevated temperatures (>673 K) [12,76,77], which suggests that selectivity to aromatics is lower at mild reaction temperatures (e.g., 473 K) regardless of gas compositions.

Taken together, Sections 3.1 and 3.2 show that even in the absence of metals, Brønsted acid sites on metal-free MFI zeolites are active for the initiation of PE and its subsequent conversion into gaseous hydrocarbons under mild reaction conditions. However, we next probe how these results differ under catalytic hydrocracking regimes with metal-loaded (Pt and Ni) MFI zeolites to elucidate the role of metal incorporation and bifunctionality, in the context of C-C bond cleavage mechanism.

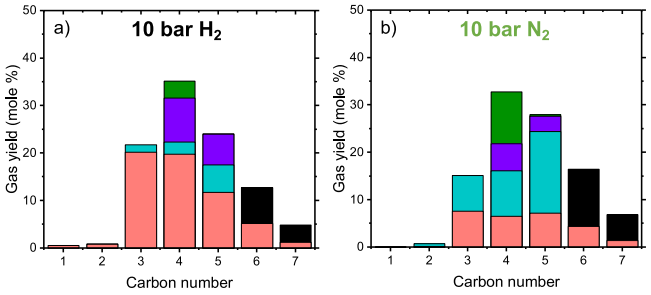

Fig. 4. Gaseous product yield (as mole percent) of C_1-C_7 for (a) H-MFI-40 (10 bar H_2) and (b) H-MFI-40 (10 bar N_2). Reaction condition: 473 K, 5 h, 1 g PE, and 0.2 g catalyst. Pink, blue, purple, and green bars indicate linear alkanes, linear alkenes, isoalkanes, and isoalkenes, respectively. Black bars indicate mixture of isoalkanes, isoalkenes, and linear alkenes for C_6-C_7 with overlapping GC peaks.

3.3. PE hydrogenolysis and hydrocracking on Pt-loaded and Ni-loaded MFI

Solid conversions and gaseous product yields were compared for the synthesized Pt- and Ni-loaded catalysts (1 wt%) for hydrogenolysis (on metal sites in the absence of acids) and hydrocracking (on metal and acid sites) of PE under similar reaction conditions with that in previous sections (473 K and 10 bar initial H_2 pressure; Fig. 5). Hydrogenolysis of gaseous alkanes on Pt and Ni is known to be structure-sensitive in the range of 1–15 nm [78–81]. Therefore, despite similar metal weight loading (1%) across SiO_2 and MFI supports, proper deconvolution of the effects of metal and acid sites on solid conversion is simplified when the series of Pt- and Ni-loaded catalysts have comparable average metal nanoparticle sizes (i.e., similar terrace to edge ratios and exposed metal surface areas). As such, we optimized our synthesis procedure to yield Pt- and Ni-catalysts with similar metal particle size distributions (e.g., SEA was used for synthesis of Ni/SiO_2 to obtain comparable metal particle sizes with Ni/MFI-40). TEM images of Pt-loaded catalysts and

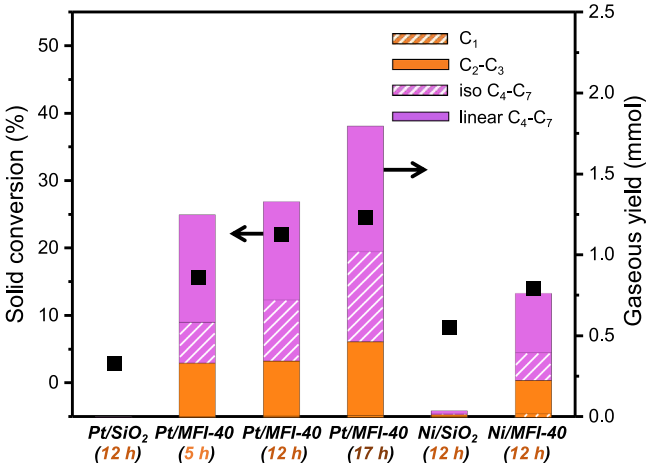

Fig. 5. Solid conversion (■) and gaseous product yield (in mmol; bars) of PE hydrogenolysis and hydrocracking on metal-loaded SiO_2 and MFI. Reaction condition: 473 K, 10 bar initial H_2 pressure, 1 g PE, and 0.2 g catalyst. Orange and purple solid bars indicate C_2-C_3 and linear C_4-C_7 alkanes, respectively. Orange and purple striped bars indicate C_1 and C_4-C_7 isoalkanes, respectively.

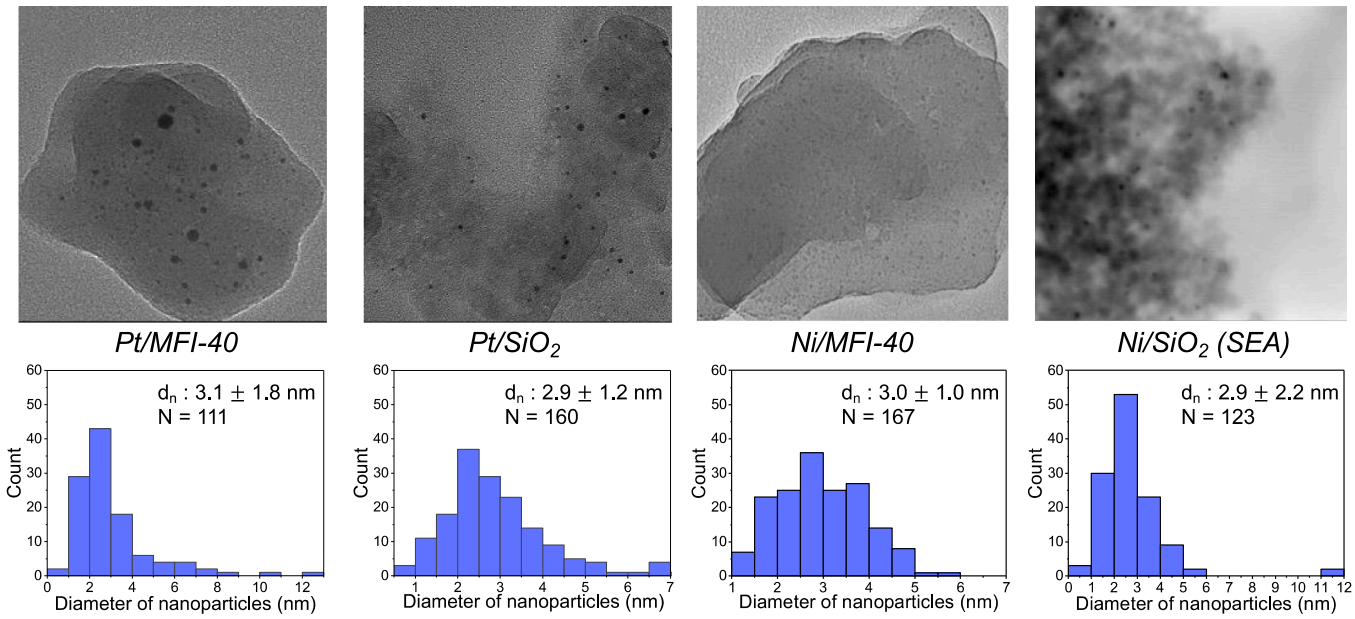

Fig. 6. Representative TEM images of (a) Pt/MFI-40, (b) Pt/SiO_2, (c) Ni/MFI-40, and (d) Ni/SiO_2 (SEA). Metal nanoparticle size distribution of each catalyst is shown below the respective TEM images.

Ni-loaded catalysts (Fig. 6) show average metal particle sizes in the range of (2.9–3.1) ± 1.5 nm and (2.9–3.0) ± 1.6 nm, respectively. Results from CO-pulse chemisorption on Pt indicate that metal particle sizes are in the range of 3.6–4.5 nm (Table S6), which agrees closely with the particle sizes determined from TEM (Fig. 6). Additionally, the metal-loaded MFI samples showed only slight decrease in micropore volumes within similar range with metal-free samples (<0.02 $cm^3\ g^{-1}$; Table 2), which suggest that loading of metal nanoparticles (1 wt%) onto MFI zeolites does not drastically alter the physical properties of the zeolite. The density of BAS on H-MFI-40 and Ni/MFI-40 are similar but slightly lower than Pt/MFI-40 by 0.10 mmol g^{-1}, which could be due to new BAS formed through ion exchange of non-acidic cations during the metal impregnation process [82]. Indeed, the effect of nuanced interactions of metal nanoparticles on acid densities will require more detailed spectroscopic interrogation in the future, but for the purpose of this study, BAS densities from NH_3-TPD are used to facilitate normalized comparisons between solid conversion and solid conversion rates of metal-loaded and metal-free zeolites.

Regardless of metal identity, solid conversions are lowest in the presence of only metal sites (3% on Pt/SiO_2 and 8% on Ni/SiO_2); the higher solid conversion on Ni/SiO_2 compared to Pt/SiO_2 can be associated with higher hydrogenolysis rates of Ni than Pt [83–86]. Solid conversions increase when both metal and acid sites are present (22% on Pt/MFI-40% and 14% on Ni/MFI-40 at 12 h), which cannot correspond to differences in metal particle sizes across the supports, as evidenced from particle size distributions (Fig. 6). Thus, this increase is likely due to the sole presence of acid sites or cooperative effects between metal and acid sites. The slightly higher solid conversion observed on Pt/MFI-40 than Ni/MFI-40 will require more detailed kinetic analysis, potentially with model compounds (e.g., hexane and decane) in flow reactors. Nonetheless, the solid conversions of both Pt/MFI-40 and Ni/MFI-40 are lower than H-MFI-40 by 7% and 15%, respectively, which are unexpected as the metal component is typically considered necessary for hydrocracking of petroleum-based feedstock (Scheme 1) [55,87,88]. In terms of gaseous product yield (Figs. 5 and S27), negligible gaseous products were observed on M/SiO_2, though Ni/SiO_2 produced larger amounts than Pt/SiO_2 (40 μmol (or 2.4 mg) on Ni/SiO_2 and 5 μmol (0.3 mg) on Pt/SiO_2), consistent with solid conversion data. The minimal amount of methane produced (<4 mol% on Ni and <0.3 mol% on Pt) on the bifunctional M/MFI-40 catalysts, again suggests that hydrogenolysis reactions on the metal sites alone are negligible in hydrocracking reactions at 473 K (Figs. S28 and S29). However, the amount of methane produced on Ni was still 3 times greater than Pt, consistent with their aforementioned hydrogenolysis affinities. Gaseous product selectivities to C_3 and C_4-C_7 on Pt/MFI-40 and Ni/MFI-40 do not vary drastically (21–28 mol% C_3 and 71–74 mol% C_4-C_7) across the range of solid conversion (14–25%) obtained on metal-loaded zeolites, but selectivity to C_1-C_2 on Ni/MFI-40 (4.7 mol%) was slightly higher than Pt/MFI-40 (1.1 mol%) at 12 h (Fig. S28). Notably, in contrast to gaseous product distributions observed on H-MFI-40 that contain small amount of alkenes, PE hydrocracking on M/MFI-40 yielded only saturated alkanes (Fig. S30), which indicates that the metal component hydrogenates the pool of alkene intermediates to a greater extent than H-MFI-40. The recovered liquid solutions from catalytic hydrocracking reactions on M/MFI-40 still showed trace presence of benzene but no alkyl-substituted aromatic rings were formed (Figs. S31 and S32), which show that the presence of metals significantly limits the formation of aromatics under a H_2 environment.

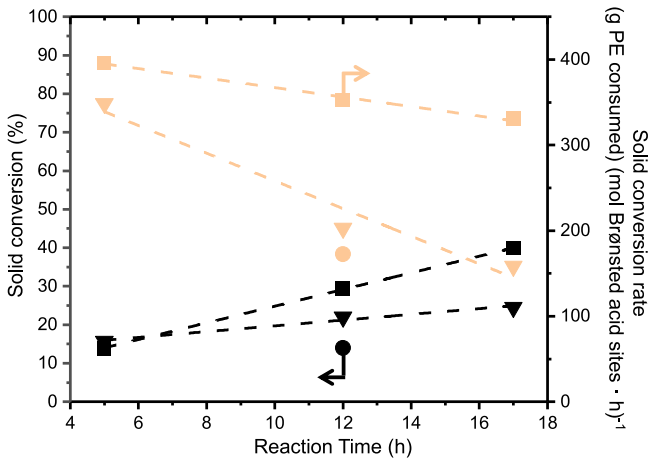

Fig. 7. Comparison of solid conversion (black symbols) and solid conversion rates (peach symbols) between metal-free H-MFI-40 (■) and metal-loaded Pt/MFI-40 (▼) and Ni/MFI-40 (●). Dashed lines are linear fits intended to guide the eye. Reaction condition: 473 K, 10 bar H_2, 1 g PE, and 0.2 g catalyst.

On Pt/MFI-40, when hydrocracking reaction time of PE increases from 5 to 17 h, solid conversion increases from 16% to 25%, while solid conversion rate decreases from 350 to 160 $\frac{gPE\ consumed}{mol\ Brønsted\ acid\ sites \bullet h}$ (Fig. 7). The decrease in solid conversion rate over time on Pt/MFI-40 is greater than that on H-MFI-40 (Fig. 7), likely due to lower quantity of alkenes present at similar reaction time due to rapid hydrogenation of alkene products (Fig. S30), in conjunction with results observed under N_2 and H_2 environments on H-MFI-40 (Fig. 4). The differences in solid conversion and product selectivity between metal-loaded and metal-free zeolites will be further contextualized in terms of the reaction mechanism in the next section.

3.4. Proposed reaction mechanism for PE hydrocracking on metal-loaded and metal-free zeolites

Collectively, the data from previous sections herein suggest that PE chains can undergo monomolecular activation on metal-free zeolites to form carbonium ions at mild reaction conditions. The relative contribution of surface protons and microporous protons, or alternatively how accessible protons are to the PE, is not explicitly invoked in previous sections. In this section, the relative contribution of surface protons and microporous protons at initial timepoints were probed using TGA experiments on pure PE and mixtures of PE + H-MFI-40 titrated with 2,4,6-TMP (denoted as H-MFI-40-TMP) under an inert (Ar) environment (temperature held constant at 523 K for 5 h) to closely monitor the mass loss of PE with respect to time. Isothermal derivative thermogravimetric (DTG) (Fig. 8) and TGA curves (Fig. S33) of pure PE resemble that of H-MFI-40-TMP, where the derivative weight loss of PE with H-MFI-40-TMP is similar compared to that of pure PE (<0.035% min^{-1}, due to slow, gradual evaporation of the melted polymer under a continuous Ar flow). This indicates that the PE is not reacting with the TMP-titrated zeolites, as external acid sites of MFI zeolites are fully titrated with TMP molecules that do not desorb at 523 K based on TGA of H-MFI-40-TMP without PE (Fig. S34). Therefore, at initial timepoints of PE cracking reactions, the bulky PE chains are likely unable to directly diffuse into the microporous voids of MFI, but instead first react with acid sites on the external surfaces of zeolites, which consequently produces smaller hydrocarbon fragments that can diffuse into the microporous voids more easily. Similarly, PE cracking reactions performed in a batch reactor on H-MFI-40-TMP also showed a 30% decrease in solid conversion when compared to H-MFI-40 that is not titrated with TMP (Fig. S35).

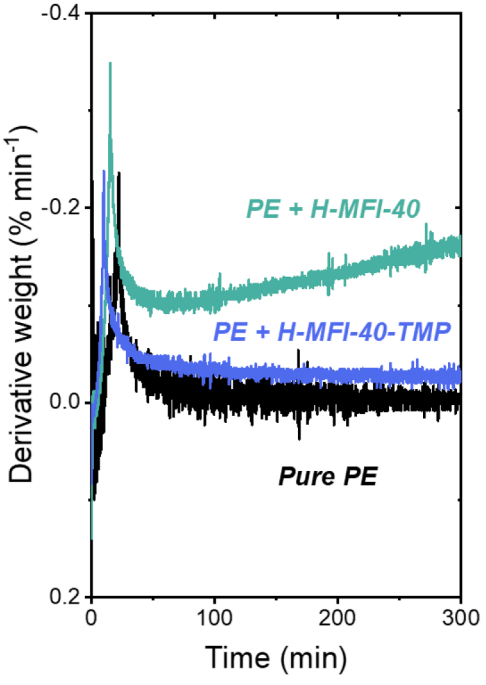

Fig. 8. Derivative weight loss curves of pure PE and mixtures of PE + TMP-titrated H-MFI-40. Samples were held at 423 K for 2 h before ramping to 523 K (time = 0 min) and held isothermally for 5 h.

Therefore, we propose that on metal-free zeolites, alkane segments along the PE chain first adsorb onto Brønsted acid sites located on external surfaces of MFI zeolites and can undergo protonation to form pentacoordinated carbonium ions. The carbonium ions can then break down into either H_2 (or CH_4, C_2H_6, and C_3H_8) and carbenium ions, which then follow the acid-catalyzed reaction pathway in Scheme 1 (red bracket) to form shorter chain hydrocarbons. The increasing amount of CH_4 and C_2H_6 products with increasing temperature (473–523 K) corroborates the existence of monomolecular activation as one of the initiation pathways, which becomes more favored with increasing temperature [64]. Although the presence of CH_4 and C_2H_6 indicates that monomolecular activation is involved in initial PE activation, parallel activation of PE through weak links (e.g., branching points, alkene groups, carbonyl) within commercial PE utilized in the study described herein is also possible. For instance, the branching points along the PE chain could lower the initial activation barrier required to form a pentacoordinated carbonium ion on Brønsted acid sites. The activation on unsaturated structure (i.e., alkenes) within PE chain is also hard to distinguish from typical beta-scission pathways of shorter-chain alkanes, and therefore, the presence of CH_4 and C_2H_6 cannot fully exclude the role of weak links in the initial activation mechanism, which can exist in parallel with monomolecular activation. Regardless, monomolecular alkane activation is likely only involved in the initial activation stage and is not the dominant pathway for which the majority of C-C bond cleavage events occur, since C_1-C_2 alkanes are present in extremely small amounts compared to C_3-C_7 products. The initial activation mechanism of alkanes on zeolites, especially at lower temperatures (<500 K), has been a topic of debate for decades. Still, a study on isobutane activation with H-MFI (SiAl = 24) has shown that isobutane readily reacts with the catalyst at 473 K to produce H_2 (and thus, the pentacoordinated carbonium ion), although the conversion remains low (i.e., 1–2%) [89]. Similarly, catalytic isomerization and cracking reactions of pentane performed at 473 K on H-MOR (SiAl = 10) and H-BEA (SiAl = 12.5) in a recirculation system show conversions greater than 5% after 120 min, providing more evidence that Brønsted acid sites can activate alkanes even under mild reaction conditions [90]. Indeed, due to the longer contact times in this study (>5 h) in our data herein, carbenium ions formed via decomposition of carbonium ions after monomolecular alkane activation (even at very low amounts) can initiate bimolecular routes or undergo beta-scission. Additionally, the long carbon chains in polymers likely have higher van der Waals interactions with the catalyst surface than gaseous and liquid hydrocarbons, which could stabilize the relevant transition states for activation of C-C bonds.

For bimolecular pathways, shorter-chain carbenium ions can activate other alkanes (or alkyl groups along the same reactant backbone) via hydride transfer, which forms new carbenium ions that can be cleaved into smaller fragments of carbenium ions and alkenes (Scheme 1). However, hydride transfer between two gaseous or liquid hydrocarbons is likely inhibited within the MFI micropores due to a larger transition state than beta-scission, as was shown for C_3-C_5 alkene/alkane mixtures [91]. Therefore, after initial activation, we propose that the PE chains undergo consecutive cleavage events on the surface acid sites until smaller chain fragments that can diffuse into micropores of MFI zeolites are formed. Because of the high selectivity to C_3-C_7 hydrocarbons and negligible $>C_{15}$ products observed across all reaction conditions probed in this study, C-C bond cleavage events within micropores likely happen at much higher rates than those on surface acid sites via beta-scission, due to higher internal acid site densities than surface densities, and potential effects of confinement. Although the potential

presence of weak links (e.g., branching points, unsaturated C-C bonds, carbonyl groups) [92,93] within commercial PE utilized in the study described herein could lower the initial activation barrier required to form a pentacoordinated carbonium ion on Brønsted acid sites or facilitate the carbenium ion cycle, this would still require initial scission to occur on surface protons and not drastically change the proposed mechanism.

On metal-loaded zeolites, the lower solid conversion observed when compared to metal-free zeolites suggest that the conventional hydrocracking mechanism proposed for gaseous and liquid alkanes (Scheme 1) might not be applicable for long-chain polymers at mild reaction conditions, but is likely dependent on the zeolite and metal properties. Considering that the bulky polymer chains diffuse significantly slower than gaseous and liquid alkanes, when an alkyl along the PE chain undergoes dehydrogenation on metal sites, the dehydrogenated alkyl on the PE chain might not be able to diffuse to neighboring acid sites in time, resulting in re-hydrogenation. In this case, the metals mainly hydrogenate the active alkenes generated from monomolecular activation or beta-scission on acid sites instead of PE activation, which consequently leads to lower solid conversion on metal-loaded zeolites. However, we note that the lower solid conversion observed herein on metal-loaded compared to metal-free zeolites do not indicate that metal-free zeolites are the most optimum choice for plastic upcycling applications, as the solid conversions observed here are sensitive to reaction conditions. For instance, in terms of catalyst recyclability and resistance to catalyst deactivation at higher reaction temperatures (>523 K), we would expect better catalyst lifetime on metal-loaded zeolites than metal-free zeolites, as the presence of metals would limit the formation of aromatics at high temperature (Fig. S36). Rather, the main takeaway from this work is that the independent role of Brønsted acid sites should be considered for catalytic hydrocracking on bifunctional catalyst, even at mild conditions, and that the ratio of alkenes to alkanes dictate PE conversion when the metal is not responsible for PE activation.

4. Conclusion

PE upcycling on metal-free and metal-loaded (i.e., Pt or Ni) MFI zeolites selectively produces mostly saturated gaseous products in the C_3-C_7 range. Solid conversion on metal-free zeolites under mild reaction conditions (473 K, 10 bar H_2) is higher than metal-loaded zeolites, which is consistent with more alkenes in the product distribution that have higher reactivity than alkanes for subsequent beta-scission into smaller fragments. This observation is further supported by the higher solid conversion observed in a N_2 environment compared to that in H_2, where N_2 favors the formation of more unsaturated species. Negligible PE degradation on physical mixtures of PE and MFI with titrated surface sites (H-MFI-40-TMP) compared to pure PE suggests that for deconstruction of bulky polymers on microporous acid supports, C-C bond cleavage events first occur at Brønsted acid sites on external surfaces, before forming smaller fragments that can diffuse into the zeolite micropores. Overall, the results and interpretations presented in this study show that catalytic cracking of PE on metal-free zeolites under both H_2 and N_2 environments is significant even at mild reaction temperatures, producing small quantities of alkenes that further catalyze C-C bond scission events in PE.

CRediT authorship contribution statement

Jun Zhi Tan: Conceptualization, Methodology, Investigation, Formal analysis, Writing – original draft, Writing – review & editing. **Cole W. Hullfish:** Investigation, Formal analysis, Writing – review & editing. **Yiteng Zheng:** Investigation, Writing – review & editing. **Bruce E. Koel:** Writing – review & editing, Supervision. **Michele L. Sarazen:** Conceptualization, Methodology, Writing – review & editing, Supervision, Project administration, Funding acquisition.

Declaration of Competing Interest

The authors declare the following financial interests/personal relationships which may be considered as potential competing interests: Michele Sarazen reports financial support was provided by US Department of Energy.

Data availability

Data will be made available on request.

Acknowledgements

This material is based upon work supported by the U.S. Department of Energy (DOE), Office of Science, Office of Basic Energy Sciences (BES), Division of Chemical Sciences, Geosciences and Biosciences through a subcontract from PNNL (FWP 78459). We acknowledge the use of Princeton's Imaging and Analysis Center, which is partially supported through the Princeton Center for Complex Materials (PCCM), a National Science Foundation (NSF)-MRSEC program (DMR-2011750).

Appendix A. Supporting information

Supplementary data associated with this article can be found in the online version at doi:10.1016/j.apcatb.2023.123028.

References

[1] Advancing Sustainable Materials Management: Facts and Figures Report, United States Environ. Prot. Agency. (2020). https://www.epa.gov/facts-and-figures-about-materials-waste-and-recycling/advancing-sustainable-materials-management (accessed June 10, 2021).
[2] Z.O.G. Schyns, M.P. Shaver, Mechanical recycling of packaging plastics: a review, Macromol. Rapid Commun. 42 (2021), 2000415, https://doi.org/10.1002/marc.202000415.
[3] S. Yin, R. Tuladhar, F. Shi, R.A. Shanks, M. Combe, T. Collister, Mechanical reprocessing of polyolefin waste: a review, Polym. Eng. Sci. 55 (2015) 2899–2909, https://doi.org/10.1002/pen.24182.
[4] T. Thiounn, R.C. Smith, Advances and approaches for chemical recycling of plastic waste, J. Polym. Sci. 58 (2020) 1347–1364, https://doi.org/10.1002/pol.20190261.
[5] M. Solis, S. Silveira, Technologies for chemical recycling of household plastics – A technical review and TRL assessment, Waste Manag 105 (2020) 128–138, https://doi.org/10.1016/j.wasman.2020.01.038.
[6] A. Piovano, E. Paone, The reductive catalytic upcycling of polyolefin plastic waste, Curr. Res. Green. Sustain. Chem. 5 (2022), 100334, https://doi.org/10.1016/j.crgsc.2022.100334.
[7] M. Chu, W. Tu, S. Yang, C. Zhang, Q. Li, Q. Zhang, J. Chen, Sustainable chemical upcycling of waste polyolefins by heterogeneous catalysis, SusMat 2 (2022) 161–185, https://doi.org/10.1002/sus2.55.
[8] S.C. Kosloski-Oh, Z.A. Wood, Y. Manjarrez, J.P. de los Rios, M.E. Fieser, Catalytic methods for chemical recycling or upcycling of commercial polymers, Mater. Horiz. 8 (2021) 1084–1129, https://doi.org/10.1039/D0MH01286F.
[9] K. Ragaert, L. Delva, K. Van Geem, Mechanical and chemical recycling of solid plastic waste, Waste Manag 69 (2017) 24–58, https://doi.org/10.1016/j.wasman.2017.07.044.
[10] J. Jiang, K. Shi, X. Zhang, K. Yu, H. Zhang, J. He, Y. Ju, J. Liu, From plastic waste to wealth using chemical recycling: a review, J. Environ. Chem. Eng. 10 (2022), 106867, https://doi.org/10.1016/j.jece.2021.106867.
[11] R. Miandad, M. Rehan, M.A. Barakat, A.S. Aburiazaiza, H. Khan, I.M.I. Ismail, J. Dhavamani, J. Gardy, A. Hassanpour, A.S. Nizami, Catalytic pyrolysis of plastic waste: Moving toward pyrolysis based biorefineries, Front. Energy Res. 7 (2019) 1–17, https://doi.org/10.3389/fenrg.2019.00027.
[12] A. Marcilla, M.I. Beltrán, R. Navarro, Thermal and catalytic pyrolysis of polyethylene over HZSM5 and HUSY zeolites in a batch reactor under dynamic conditions, Appl. Catal. B Environ. 86 (2009) 78–86, https://doi.org/10.1016/j.apcatb.2008.07.026.
[13] R. Bagri, P.T. Williams, Catalytic pyrolysis of polyethylene, J. Anal. Appl. Pyrolysis 63 (2002) 29–41, https://doi.org/10.1016/S0165-2370(01)00139-5.
[14] S. Klaimy, C. Ciotonea, J. Dhainaut, S. Royer, M. Casetta, S. Duquesne, G. Tricot, J.-F. Lamonier, Flash catalytic pyrolysis of polyethylene over (Alumino)silicate materials, ChemCatChem 12 (2020) 1109–1116, https://doi.org/10.1002/cctc.201901819.
[15] K. Praveen Kumar, S. Srinivas, Catalytic Co-pyrolysis of biomass and plastics (polypropylene and polystyrene) using spent FCC catalyst, Energy Fuels 34 (2020) 460–473, https://doi.org/10.1021/acs.energyfuels.9b03135.

[16] P.N. Sharratt, Y.-H. Lin, A.A. Garforth, J. Dwyer, Investigation of the catalytic pyrolysis of high-density polyethylene over a HZSM-5 catalyst in a laboratory fluidized-bed reactor, Ind. Eng. Chem. Res. 36 (1997) 5118–5124, https://doi.org/10.1021/ie970348b.

[17] D. Zhao, X. Wang, J.B. Miller, G.W. Huber, The chemistry and kinetics of polyethylene pyrolysis: a process to produce fuels and chemicals, ChemSusChem 13 (2020) 1764–1774, https://doi.org/10.1002/cssc.201903434.

[18] I. Vollmer, M.J.F. Jenks, M.C.P. Roelands, R.J. White, T. van Harmelen, P. de Wild, G.P. van der Laan, F. Meirer, J.T.F. Keurentjes, B.M. Weckhuysen, Beyond Mechanical Recycling: Giving New Life to Plastic Waste, Angew. Chem. Int. Ed. 59 (2020) 15402–15423, https://doi.org/10.1002/anie.201915651.

[19] P.R. Robinson, G.E. Dolbear, in: C.S. Hsu, P.R. Robinson (Eds.), Hydrotreating and Hydrocracking: Fundamentals BT - Practical Advances in Petroleum Processing, Springer, New York, New York, NY, 2006, pp. 177–218, https://doi.org/10.1007/978-0-387-25789-1_7.

[20] R.F. Sullivan, J.W. Scott, The Development of Hydrocracking, in: Heterog. Catal., American Chemical Society, 1983, pp. 24–293, https://doi.org/10.1021/bk-1983-0222.ch024.

[21] J.W. Ward, Hydrocracking processes and catalysts, Fuel Process. Technol. 35 (1993) 55–85, https://doi.org/10.1016/0378-3820(93)90085-I.

[22] G.C. Bond (Ed.), Introduction to the Catalysis of Hydrocarbon Reactions BT - Metal-Catalysed Reactions of Hydrocarbons, Springer, US, Boston, MA, 2005, pp. 209–255, https://doi.org/10.1007/0-387-26111-7_5.

[23] A. Marcilla, M.I. Beltrán, F. Hernández, R. Navarro, HZSM5 and HUSY deactivation during the catalytic pyrolysis of polyethylene, Appl. Catal. A Gen. 278 (2004) 37–43, https://doi.org/10.1016/j.apcata.2004.09.023.

[24] A.K. Panda, R.K. Singh, Catalytic performances of kaoline and silica alumina in the thermal degradation of polypropylene, J. Fuel Chem. Technol. 39 (2011) 198–202, https://doi.org/10.1016/S1872-5813(11)60017-0.

[25] H. Ohkita, R. Nishiyama, Y. Tochihara, T. Mizushima, N. Kakuta, Y. Morioka, A. Ueno, Y. Namiki, S. Tanifuji, H. Katoh, H. Sunazuka, R. Nakayama, T. Kuroyanagi, Acid properties of silica-alumina catalysts and catalytic degradation of polyethylene, Ind. Eng. Chem. Res. 32 (1993) 3112–3116, https://doi.org/10.1021/ie00024a021.

[26] S. Gopinath, P.K. Devan, K. Pitchandi, Production of pyrolytic oil from ULDP plastics using silica-alumina catalyst and used as fuel for DI diesel engine, RSC Adv. 10 (2020) 37266–37279, https://doi.org/10.1039/D0RA07073D.

[27] A.K. Panda, A. Alotaibi, I.V. Kozhevnikov, N.R. Shiju, Pyrolysis of plastics to liquid fuel using sulphated zirconium hydroxide catalyst, Waste Biomass-.-. Valoriz. 11 (2020) 6337–6345, https://doi.org/10.1007/s12649-019-00841-4.

[28] K.R. Venkatesh, J. Hu, W. Wang, G.D. Holder, J.W. Tierney, I. Wender, Hydrocracking and hydroisomerization of long-chain alkanes and polyolefins over metal-promoted anion-modified zirconium oxides, Energy Fuels 10 (1996) 1163–1170, https://doi.org/10.1021/ef960049j.

[29] J. Shabtai, X. Xiao, W. Zmierczak, Depolymerization−Liquefaction of Plastics and Rubbers. 1. Polyethylene, Polypropylene, and Polybutadiene, Energy Fuels 11 (1997) 76–87, https://doi.org/10.1021/ef960076.

[30] A.J. Martín, C. Mondelli, S.D. Jaydev, J. Pérez-Ramírez, Catalytic processing of plastic waste on the rise, Chem 7 (2021) 1487–1533, https://doi.org/10.1016/j.chempr.2020.12.006.

[31] J.E. Rorrer, G.T. Beckham, Y. Román-Leshkov, Conversion of polyolefin waste to liquid alkanes with ru-based catalysts under mild conditions, JACS Au 1 (2021) 8–12, https://doi.org/10.1021/jacsau.0c00041.

[32] J.E. Rorrer, C. Troyano-Valls, G.T. Beckham, Y. Román-Leshkov, Hydrogenolysis of polypropylene and mixed polyolefin plastic waste over Ru/C to produce liquid alkanes, ACS Sustain. Chem. Eng. 9 (2021) 11661–11666, https://doi.org/10.1021/acssuschemeng.1c03786.

[33] A. Bin Jumah, V. Anbumuthu, A.A. Tedstone, A.A. Garforth, Catalyzing the hydrocracking of low density polyethylene, Ind. Eng. Chem. Res. 58 (2019) 20601–20609, https://doi.org/10.1021/acs.iecr.9b04263.

[34] A. Bin Jumah, A.A. Tedstone, A.A. Garforth, Hydrocracking of virgin and post-consumer polymers, Microporous Mesoporous Mater. 315 (2021), 110912, https://doi.org/10.1016/j.micromeso.2021.110912.

[35] A. Bin Jumah, M. Malekshahian, A.A. Tedstone, A.A. Garforth, Kinetic modeling of hydrocracking of low-density polyethylene in a batch reactor, ACS Sustain. Chem. Eng. 9 (2021) 16757–16769, https://doi.org/10.1021/acssuschemeng.1c06231.

[36] C. Jia, S. Xie, W. Zhang, N.N. Intan, J. Sampath, J. Pfaendtner, H. Lin, Deconstruction of high-density polyethylene into liquid hydrocarbon fuels and lubricants by hydrogenolysis over Ru catalyst, Chem. Catal. 1 (2021) 437–455, https://doi.org/10.1016/j.checat.2021.04.002.

[37] Z. Dong, W. Chen, K. Xu, Y. Liu, J. Wu, F. Zhang, Understanding the structure–activity relationships in catalytic conversion of polyolefin plastics by zeolite-based catalysts: a critical review, ACS Catal. 12 (2022) 14882–14901, https://doi.org/10.1021/acscatal.2c04915.

[38] W.-T. Lee, A. van Muyden, F.D. Bobbink, M.D. Mensi, J.R. Carullo, P.J. Dyson, Mechanistic classification and benchmarking of polyolefin depolymerization over silica-alumina-based catalysts, Nat. Commun. 13 (2022) 4850, https://doi.org/10.1038/s41467-022-32563-y.

[39] C. Wang, T. Xie, P.A. Kots, B.C. Vance, K. Yu, P. Kumar, J. Fu, S. Liu, G. Tsilomelekis, E.A. Stach, W. Zheng, D.G. Vlachos, Polyethylene Hydrogenolysis at Mild Conditions over Ruthenium on Tungstated Zirconia, JACS Au 1 (2021) 1422–1434, https://doi.org/10.1021/jacsau.1c00200.

[40] S. Liu, P.A. Kots, B.C. Vance, A. Danielson, D.G. Vlachos, Plastic waste to fuels by hydrocracking at mild conditions, Sci. Adv. 7 (2021) eabf8283, https://doi.org/10.1126/sciadv.abf8283.

[41] P.A. Kots, S. Liu, B.C. Vance, C. Wang, J.D. Sheehan, D.G. Vlachos, Polypropylene plastic waste conversion to lubricants over Ru/TiO2 catalysts, ACS Catal. 11 (2021) 8104–8115, https://doi.org/10.1021/acscatal.1c00874.

[42] B.C. Vance, P.A. Kots, C. Wang, Z.R. Hinton, C.M. Quinn, T.H. Epps, L.T.J. Korley, D.G. Vlachos, Single pot catalyst strategy to branched products via adhesive isomerization and hydrocracking of polyethylene over platinum tungstated zirconia, Appl. Catal. B Environ. 299 (2021), 120483, https://doi.org/10.1016/j.apcatb.2021.120483.

[43] G. Celik, R.M. Kennedy, R.A. Hackler, M. Ferrandon, A. Tennakoon, S. Patnaik, A. M. Lapointe, S.C. Ammal, A. Heyden, F.A. Perras, M. Pruski, S.L. Scott, K. R. Poeppelmeier, A.D. Sadow, M. Delferro, Upcycling single-use polyethylene into high-quality liquid products, ACS Cent. Sci. 5 (2019) 1795–1803, https://doi.org/10.1021/acscentsci.9b00722.

[44] L. Chen, L.C. Meyer, L. Kovarik, D. Meira, X.I. Pereira-Hernandez, H. Shi, K. Khivantsev, O.Y. Gutiérrez, J. Szanyi, Disordered, Sub-Nanometer Ru Structures on CeO2 are Highly Efficient and Selective Catalysts in Polymer Upcycling by Hydrogenolysis, ACS Catal. 12 (2022) 4618–4627, https://doi.org/10.1021/acscatal.2c00684.

[45] L. Chen, Y. Zhu, L.C. Meyer, L.V. Hale, T.T. Le, A. Karkamkar, J.A. Lercher, O. Y. Gutiérrez, J. Szanyi, Effect of reaction conditions on the hydrogenolysis of polypropylene and polyethylene into gas and liquid alkanes, React. Chem. Eng. 7 (2022) 844–854, https://doi.org/10.1039/D1RE00431J.

[46] A. Tennakoon, X. Wu, A.L. Paterson, S. Patnaik, Y. Pei, A.M. LaPointe, S.C. Ammal, R.A. Hackler, A. Heyden, I.I. Slowing, G.W. Coates, M. Delferro, B. Peters, W. Huang, A.D. Sadow, F.A. Perras, Catalytic upcycling of high-density polyethylene via a processive mechanism, Nat. Catal. 3 (2020) 893–901, https://doi.org/10.1038/s41929-020-00519-4.

[47] J.E. Rorrer, A.M. Ebrahim, Y. Questell-Santiago, J. Zhu, C. Troyano-Valls, A. S. Asundi, A.E. Brenner, S.R. Bare, C.J. Tassone, G.T. Beckham, Y. Román-Leshkov, Role of bifunctional Ru/Acid catalysts in the selective hydrocracking of polyethylene and polypropylene waste to liquid hydrocarbons, ACS Catal. 12 (2022) 13969–13979, https://doi.org/10.1021/acscatal.2c03596.

[48] S. Gao, L.D. Schmidt, Effect of oxidation-reduction cycling on C2H6 hydrogenolysis: Comparison of Ru, Rh, Ir, Ni, Pt, and Pd on SiO2, J. Catal. 115 (1989) 356–364, https://doi.org/10.1016/0021-9517(89)90040-7.

[49] D. Guo, X. Liu, F. Cheng, W. Zhao, S. Wen, Y. Xiang, Q. Xu, N. Yu, D. Yin, Selective hydrogenolysis of 5-hydroxymethylfurfural to produce biofuel 2, 5-dimethylfuran over Ni/ZSM-5 catalysts, Fuel 274 (2020), 117853, https://doi.org/10.1016/j.fuel.2020.117853.

[50] F. Mauriello, E. Paone, R. Pietropaolo, A.M. Balu, R. Luque, Catalytic transfer hydrogenolysis of lignin-derived aromatic ethers promoted by bimetallic Pd/Ni systems, ACS Sustain. Chem. Eng. 6 (2018) 9269–9276, https://doi.org/10.1021/acssuschemeng.8b01593.

[51] H. Taghvaei, M.R. Rahimpour, P. Bruggeman, Catalytic hydrodeoxygenation of anisole over nickel supported on plasma treated alumina–silica mixed oxides, RSC Adv. 7 (2017) 30990–30998, https://doi.org/10.1039/C7RA02594G.

[52] A. Von Held Soares, H. Atia, U. Armbruster, F.B. Passos, A. Martin, Platinum, palladium and nickel supported on Fe3O4 as catalysts for glycerol aqueous-phase hydrogenolysis and reforming, Appl. Catal. A Gen. 548 (2017) 179–190, https://doi.org/10.1016/j.apcata.2017.07.023.

[53] J. Duan, W. Chen, C. Wang, L. Wang, Z. Liu, X. Yi, W. Fang, H. Wang, H. Wei, S. Xu, Y. Yang, Q. Yang, Z. Bao, Z. Zhang, Q. Ren, H. Zhou, X. Qin, A. Zheng, F.-S. Xiao, Coking-Resistant Polyethylene Upcycling Modulated by Zeolite Micropore Diffusion, J. Am. Chem. Soc. 144 (2022) 14269–14277, https://doi.org/10.1021/jacs.2c05125.

[54] G. Zichittella, A.M. Ebrahim, J. Zhu, A.E. Brenner, G. Drake, G.T. Beckham, S. R. Bare, J.E. Rorrer, Y. Román-Leshkov, Hydrogenolysis of Polyethylene and Polypropylene into Propane over Cobalt-Based Catalysts, JACS Au 2 (2022) 2259–2268, https://doi.org/10.1021/jacsau.2c00402.

[55] J. Weitkamp, Catalytic Hydrocracking—Mechanisms and Versatility of the Process, ChemCatChem 4 (2012) 292–306, https://doi.org/10.1002/cctc.201100315.

[56] D.T. Bregante, D.S. Potts, O. Kwon, E.Z. Ayla, J.Z. Tan, D.W. Flaherty, Effects of Hydrofluoric Acid Concentration on the Density of Silanol Groups and Water Adsorption in Hydrothermally Synthesized Transition-Metal-Substituted Silicalite-1, Chem. Mater. 32 (2020) 7425–7437, https://doi.org/10.1021/acs.chemmater.0c02405.

[57] A. Wong, Q. Liu, S. Griffin, A. Nicholls, J.R. Regalbuto, Synthesis of ultrasmall, homogeneously alloyed, bimetallic nanoparticles on silica supports, Science 358 (2017) 1427–1430, https://doi.org/10.1126/science.aao6538.

[58] M.L. Sarazen, E. Doskocil, E. Iglesia, Effects of void environment and acid strength on alkene oligomerization selectivity, ACS Catal. 6 (2016) 7059–7070, https://doi.org/10.1021/acscatal.6b02128.

[59] V. Zholobenko, C. Freitas, M. Jendrlin, P. Bazin, A. Travert, F. Thibault-Starzyk, Probing the acid sites of zeolites with pyridine: Quantitative AGIR measurements of the molar absorption coefficients, J. Catal. 385 (2020) 52–60, https://doi.org/10.1016/j.jcat.2020.03.003.

[60] O.A. Abdelrahman, K.P. Vinter, L. Ren, D. Xu, R.J. Gorte, M. Tsapatsis, P. J. Dauenhauer, Simple quantification of zeolite acid site density by reactive gas chromatography, Catal. Sci. Technol. 7 (2017) 3831–3841, https://doi.org/10.1039/C7CY01068K.

[61] P. Hudec, A. Smiešková, Z. Idek, P. Schneider, O. Ŝolcová, Determination of microporous structure of zeolites by t-plot method—State-of-the-art, in, in: R. Aiello, G. Giordano, F.B.T.-S. in S.S., C. Testa (Eds.), Impact Zeolites Other Porous Mater. New Technol. Begin. New Millenn, Elsevier, 2002, pp. 1587–1594, https://doi.org/10.1016/S0167-2991(02)80328-7.

[62] R. Gounder, E. Iglesia, Catalytic Consequences of Spatial Constraints and Acid Site Location for Monomolecular Alkane Activation on Zeolites, J. Am. Chem. Soc. 131 (2009) 1958–1971, https://doi.org/10.1021/ja808292c.
[63] J. Meusinger, A. Corma, Activation of Hydrogen on Zeolites: Kinetics and Mechanism of n-Heptane Cracking on H-ZSM-5 Zeolites Under High Hydrogen Pressure, J. Catal. 152 (1995) 189–197, https://doi.org/10.1006/jcat.1995.1072.
[64] S. Kotrel, H. Knözinger, B.C. Gates, The Haag–Dessau mechanism of protolytic cracking of alkanes, Microporous Mesoporous Mater. 35– 36 (2000) 11–20, https://doi.org/10.1016/S1387-1811(99)00204-8.
[65] B.S. Greensfelder, H.H. Voge, G.M. Good, Catalytic and thermal cracking of pure hydrocarbons: mechanisms of reaction, Ind. Eng. Chem. 41 (1949) 2573–2584, https://doi.org/10.1021/ie50479a043.
[66] P.M. Kester, E. Iglesia, R. Gounder, Parallel Alkane Dehydrogenation Routes on Brønsted Acid and Reaction-Derived Carbonaceous Active Sites in Zeolites, J. Phys. Chem. C. 124 (2020) 15839–15855, https://doi.org/10.1021/acs.jpcc.0c01808.
[67] Y.V. Kissin, Relative reactivities of alkanes in catalytic cracking reactions, J. Catal. 126 (1990) 600–609, https://doi.org/10.1016/0021-9517(90)90023-D.
[68] D.M. Nace, Catalytic cracking over crystalline aluminosilicates. II. Application of microreactor technique to investigation of structural effects of hydrocarbon reactants, Ind. Eng. Chem. Prod. Res. Dev. 8 (1969) 31–38, https://doi.org/10.1021/i360029a005.
[69] A. Janda, A.T. Bell, Effects of Si/Al Ratio on the Distribution of Framework Al and on the Rates of Alkane Monomolecular Cracking and Dehydrogenation in H-MFI, J. Am. Chem. Soc. 135 (2013) 19193–19207, https://doi.org/10.1021/ja4081937.
[70] G. Noh, Z. Shi, S.I. Zones, E. Iglesia, Isomerization and β-scission reactions of alkanes on bifunctional metal-acid catalysts: Consequences of confinement and diffusional constraints on reactivity and selectivity, J. Catal. 368 (2018) 389–410, https://doi.org/10.1016/j.jcat.2018.03.033.
[71] W.O. Haag, R.M. Dessau, Proc. 8th. Int. Congr. Catal, Berlin, 2, Verlag Chemie, Weinheim, 1984, p. 305.
[72] P. Magnoux, P. Roger, C. Canaff, V. Fouche, N.S. Gnep, M. Guisnet, New Technique for the Characterization of Carbonaceous Compounds Responsible for Zeolite Deactivation, in: B. Delmon, G.F.B.T.-S. in S.S., C. Froment (Eds.), Catal. Deactiv, Elsevier, 1987, pp. 317–330, https://doi.org/10.1016/S0167-2991(09)60370-0.
[73] G.R. Bamwenda, Y.X. Zhao, B.W. Wojciechowski, The influence of reaction temperature on the cracking mechanism of 2-methylhexane, J. Catal. 148 (1994) 595–606, https://doi.org/10.1006/jcat.1994.1246.
[74] J. Abbot, A. Corma, B.W. Wojciechowski, The catalytic isomerization of 1-hexene on H-ZSM-5 zeolite: The effects of a shape-selective catalyst, J. Catal. 92 (1985) 398–408, https://doi.org/10.1016/0021-9517(85)90273-8.
[75] R. Gounder, E. Iglesia, Catalytic hydrogenation of alkenes on acidic zeolites: Mechanistic connections to monomolecular alkane dehydrogenation reactions, J. Catal. 277 (2011) 36–45, https://doi.org/10.1016/j.jcat.2010.10.013.
[76] S.L. Wong, S. Armenise, B.B. Nyakuma, A. Bogush, S. Towers, C.H. Lee, K.Y. Wong, T.H. Lee, E. Rebrov, M. Muñoz, Plastic pyrolysis over HZSM-5 zeolite and fluid catalytic cracking catalyst under ultra-fast heating, J. Anal. Appl. Pyrolysis 169 (2023), 105793, https://doi.org/10.1016/j.jaap.2022.105793.
[77] M. Seitz, S. Schröter, Catalytic Depolymerization of Polyolefinic Plastic Waste, Chem. Ing. Tech. 94 (2022) 720–726, https://doi.org/10.1002/cite.202100182.
[78] H. Shi, O.Y. Gutiérrez, H. Yang, N.D. Browning, G.L. Haller, J.A. Lercher, Catalytic Consequences of Particle Size and Chloride Promotion in the Ring-Opening of Cyclopentane on Pt/Al2O3, ACS Catal. 3 (2013) 328–338, https://doi.org/10.1021/cs300636j.
[79] H. Glassl, K. Hayek, R. Kramer, Electron microscopy of PtAl2O3 model catalysts: III. The hydrogenolysis of methylcyclopentane as a function of particle size, J. Catal. 68 (1981) 397–405, https://doi.org/10.1016/0021-9517(81)90109-3.
[80] A. Sárkány, P. Tétényi, On the structure sensitivity of ethane hydrogenolysis on Ni catalysts, React. Kinet. Catal. Lett. 12 (1979) 297–301, https://doi.org/10.1007/BF02064259.
[81] M.F. Guilleux, J.A. Dalmon, G.A. Martin, Mechanism and structure sensitivity of propane hydrogenolysis over Ni/SiO2 catalysts, J. Catal. 62 (1980) 235–242, https://doi.org/10.1016/0021-9517(80)90451-0.
[82] D. Kubička, N. Kumar, T. Venäläinen, H. Karhu, I. Kubičková, H. Österholm, D. Y. Murzin, Metal−Support Interactions in Zeolite-Supported Noble Metals: Influence of Metal Crystallites on the Support Acidity, J. Phys. Chem. B. 110 (2006) 4937–4946, https://doi.org/10.1021/jp055754k.
[83] A. Almithn, D. Hibbitts, Comparing Rate and Mechanism of Ethane Hydrogenolysis on Transition-Metal Catalysts, J. Phys. Chem. C. 123 (2019) 5421–5432, https://doi.org/10.1021/acs.jpcc.8b11070.
[84] G. Leclercq, L. Leclercq, L.M. Bouleau, S. Pietrzyk, R. Maurel, Hydrogenolysis of saturated hydrocarbons: IV. Kinetics of the hydrogenolysis of ethane, propane, butane, and isobutane over nickel, J. Catal. 88 (1984) 8–17, https://doi.org/10.1016/0021-9517(84)90044-7.
[85] H. Matsumoto, Y. Saito, Y. Yoneda, Contrast between nickel and platinum catalysts in hydrogenolysis of saturated hydrocarbons, J. Catal. 19 (1970) 101–112, https://doi.org/10.1016/0021-9517(70)90272-1.
[86] G. Leclercq, S. Pietrzyk, M. Peyrovi, M. Karroua, Hydrogenolysis of saturated hydrocarbons: V. Influence of hydrocarbon structures on the activity and selectivity of Ni on silica, J. Catal. 99 (1986) 1–11, https://doi.org/10.1016/0021-9517(86)90192-2.
[87] G.A. Mills, H. Heinemann, T.H. Milliken, A.G. Oblad, Houdriforming reactions) catalytic mechanism, Ind. Eng. Chem. 45 (1953) 134–137, https://doi.org/10.1021/ie50517a043.
[88] J. Scherzer, A.J. Gruia, Hydrocracking Science and Technology, 1st Editio, CRC Press,, Boca Raton, 1996, https://doi.org/10.1201/9781482233889.
[89] B. Louis, M.M. Pereira, F.M. Santos, P.M. Esteves, J. Sommer, Alkane Activation over Acidic Zeolites: The First Step, Chem. – A Eur. J. 16 (2010) 573–576, https://doi.org/10.1002/chem.200901737.
[90] T. Wakayama, H. Matsuhashi, Reaction of linear, branched, and cyclic alkanes catalyzed by Brönsted and Lewis acids on H-mordenite, H-beta, and sulfated zirconia, J. Mol. Catal. A Chem. 239 (2005) 32–40, https://doi.org/10.1016/j.molcata.2005.05.031.
[91] M.L. Sarazen, E. Iglesia, Experimental and theoretical assessment of the mechanism of hydrogen transfer in alkane-alkene coupling on solid acids, J. Catal. 354 (2017) 287–298, https://doi.org/10.1016/j.jcat.2017.08.002.
[92] J.D. Peterson, S. Vyazovkin, C.A. Wight, Kinetics of the thermal and thermo-oxidative degradation of polystyrene, polyethylene and poly(propylene), Macromol. Chem. Phys. 202 (2001) 775–784, https://doi.org/10.1002/1521-3935(20010301)202:6<775::AID-MACP775>3.0.CO;2-G.
[93] W.L. Hawkins, in: W.L. Hawkins (Ed.), Polymer Degradation BT - Polymer Degradation and Stabilization, Springer Berlin Heidelberg, Berlin, Heidelberg, 1984, pp. 3–34, https://doi.org/10.1007/978-3-642-69376-2_2.